Nanoscale

RSC Publishing

FEATURE ARTICLE

View Article Online
View Journal | View Issue

Magnetic particle imaging: advancements and perspectives for real-time *in vivo* monitoring and image-guided therapy

Cite this: *Nanoscale*, 2013, **5**, 4040

Michele H. Pablico-Lansigan, Shu F. Situ and Anna Cristina S. Samia*

Magnetic particle imaging (MPI) is an emerging biomedical imaging technology that allows the direct quantitative mapping of the spatial distribution of superparamagnetic iron oxide nanoparticles. MPI's increased sensitivity and short image acquisition times foster the creation of tomographic images with high temporal and spatial resolution. The contrast and sensitivity of MPI is envisioned to transcend those of other medical imaging modalities presently used, such as magnetic resonance imaging (MRI), X-ray scans, ultrasound, computed tomography (CT), positron emission tomography (PET) and single photon emission computed tomography (SPECT). In this review, we present an overview of the recent advances in the rapidly developing field of MPI. We begin with a basic introduction of the fundamentals of MPI, followed by some highlights over the past decade of the evolution of strategies and approaches used to improve this new imaging technique. We also examine the optimization of iron oxide nanoparticle tracers used for imaging, underscoring the importance of size homogeneity and surface engineering. Finally, we present some future research directions for MPI, emphasizing the novel and exciting opportunities that it offers as an important tool for real-time *in vivo* monitoring. All these opportunities and capabilities that MPI presents are now seen as potential breakthrough innovations in timely disease diagnosis, implant monitoring, and image-guided therapeutics.

Received 30th January 2013
Accepted 17th March 2013

DOI: 10.1039/c3nr00544e

www.rsc.org/nanoscale

Introduction

Over the past decade, extensive efforts have been devoted to developing "theranostics," techniques to combine therapeutic

Department of Chemistry, Case Western Reserve University, 10900 Euclid Avenue, Cleveland, Ohio, 44106 USA. E-mail: anna.samia@case.edu; Fax: +1 (216)368-3006; Tel: +1 (216)368-3852

Michele H. Pablico-Lansigan received her B.S. degree in Chemistry at the University of the Philippines in Los Banos, Laguna in 2002. She then spent three years teaching as a full-time instructor at the same university where she taught General Chemistry and Physical Chemistry laboratory courses. In 2005, she was accepted as a graduate fellow at Georgetown University where she worked with Dr Sarah L. Stoll on manganese and manganese–iron oxo clusters and evaluated their use as potential contrast agents for magnetic resonance imaging. After obtaining her Ph.D. degree in 2011, she moved to Cleveland, Ohio to pursue postdoctoral work under the supervision of Dr Anna Cristina S. Samia at Case Western Reserve University where her research interest focuses on magnetic-polymer hybrid nanostructures for theranostic applications.

Shu F. Situ is a Ph.D. student at the Department of Chemistry at Case Western Reserve University. She received her Bachelor of Science in Chemistry degree in 2011 from the University of Michigan, Ann Arbor. She joined Dr Samia's research group in 2012. Her current research projects focus on developing magnetic-polymer nanocomposites for biomedical imaging.

and diagnostic functions in single platforms, to improve the efficacy and success rate of treatments.[1–4] Central to the progress of theranostic research and development are novel imaging technologies that use specially designed probes to enable the acquisition of high-resolution images to guide the treatment process.[1–3,5–10] In particular, tomographic imaging, has become an indispensable tool for visualizing lesions, monitoring blood flow, and discriminating normal from diseased tissues in the human body.[11] To achieve accurate diagnoses and to detect diseases at their earliest stages, it is crucial that adapted imaging techniques are highly sensitive.[4] This ensures timely monitoring of illnesses and planning of subsequent treatment procedures. Among the frequently used tomographic imaging techniques in the clinic are magnetic resonance imaging (MRI),[6,7,12] computed tomography (CT),[13] positron emission tomography (PET)[14] and single photon emission computed tomography (SPECT).[15] Each of these imaging modalities has strengths and weaknesses, but nevertheless all remain valuable tools for the medical diagnosis and treatment.

Magnetic particle imaging (MPI), an emerging tomographic imaging method, directly measures the magnetization of iron oxide nanoparticle tracers. Pioneered at the turn of the millennium by Gleich and Weizenecker at the Philips Research Laboratories in Hamburg,[16–19] MPI is sensitive and fast, and offers high spatial and temporal resolutions.[11,20] The MPI signal is derived from the nonlinear re-magnetization response of superparamagnetic iron oxide nanoparticles (SPIONs) to an oscillating magnetic field.[18–20] The signal generated by the changing magnetization of the SPION tracers results in the occurrence of higher order harmonics of the excitation frequency, which facilitates the quantitative mapping of the local distribution of the magnetic nanoparticles at high spatial and temporal resolution.[4,17,21] Since tissue and organ components are diamagnetic, they appear transparent in MPI measurements, eliminating problems associated with background signals and resulting in images with exceptional positive contrast.[4,17,18,21] Moreover, MPI scans are typically conducted at low frequency magnetic fields, which leads to zero attenuation, implying that this imaging method is quantitative at any depth.[18]

In contrast to other imaging modalities such as X-ray scans, CT, PET and SPECT, MPI does not use any ionizing radiation and is thus non-invasive and highly suitable for routine diagnostic procedures.[22] Because it is non-invasive and uses SPION tracers and magnetic field responses to generate images, MPI is often compared to MRI.[23] However, unlike MRI the image intensity obtained in MPI is *directly* related to the amount and location of the SPION tracers. In comparison, MRI *indirectly* probes the SPION response by detecting the dephasing of proton spins of the surrounding water molecules to produce images.[24,25] In addition, MPI scans are obtained more rapidly than MRI scans, offering better potential for real-time *in vivo* imaging and monitoring applications.[17,20,26] Weizenecker *et al.*[27] demonstrated this potential when they obtained the first *in vivo* 3D real-time MPI scans revealing the details of a beating mouse heart. Although still in its nascent stage, MPI is being pursued for potential applications in diagnostic imaging of cardiovascular systems, dynamic assessments of myocardial perfusion, labelling and tracking of cells for oncologic investigations,[17] and study of prosthesis wear in joint implants, among others. With its unique combination of properties and capabilities, MPI is expected to compete with other established tomographic imaging modalities routinely used in the medical field.

Supplementing MPI's advantages, SPIONs exploited as MPI tracers offer exceptional frameworks for theranostic applications because they are non-toxic, demonstrate distinctive responses to external magnetic fields, and have a long history of use for bio-imaging and therapeutic purposes.[28–33] Over the years, the use of SPIONs in biomedical applications has been well-documented – as contrast agents for MRI,[6] as multi-modal drug delivery vehicles for cancer treatment,[9] and as therapeutic systems for magnetic hyperthermia.[34] Regarded as important nanoparticle platforms, SPIONs are versatile probes in biomedical research because their intrinsic magnetic properties can be remotely triggered and easily tuned.[35,36] In addition, the synthesis and functionalization of SPIONs have been widely studied and substantial progress to control their size, shape, and surface properties have been reported by various research groups.[37–48] Since MPI utilizes SPIONs as tracer material, it provides an advantage over other imaging platforms: SPIONs can be used as visualizing tools for diagnostic tests and employed in an image-guided therapeutic mode.[4] This dual use is accomplished by using innovatively engineered iron oxide nanoparticles.[1–3,5–10] Currently, the number of reports on the research and development of suitable magnetic nanoparticle tracers for MPI are increasing.[22,26,49–52]

From its inception in 2001, MPI has seen significant improvements, ranging from the evolution of hardware and image reconstruction methods to the design of magnetic nanoparticle tracers and their applications. In this review, we will provide an account of the development of MPI as a robust imaging method for biomedical applications. This will include an overview of the principles of this new imaging modality, the rationale underlying the sensitivity of the technique, and the innovative engineering of magnetic nanoparticle tracers.

Anna Cristina S. Samia is an Assistant Professor at the Department of Chemistry at Case Western Reserve University. She received her Ph.D. degree from the Georgia Institute of Technology in 2002 under the supervision of Z. John Zhang. She continued her research training as a Postdoctoral Research Associate at Argonne National Laboratory under the direction of Dr Xiao-Min Lin and then worked as a Research Fellow at Case Western Reserve University. Her current research interests include the synthesis of composite magnetic nanomaterials for applications in bio-imaging and biosensing.

Importantly, we focus on MPI's promising applications in real-time *in vivo* monitoring as well as on its pivotal role in image-guided therapy and advanced theranostics. For more detailed accounts on the physics, image reconstruction, hardware fabrication, MPI tracer design and applications, readers are recommended to consult the comprehensive books written by Knopp *et al.*[11] and Buzug *et al.*[53]

Development and current state-of-the-art of magnetic particle imaging (MPI)

The concept of MPI was originally conceived by Gleich in 2001 at the Philips Research Laboratory in Hamburg, Germany.[11] In a seminal paper four years later Gleich and Weizenecker reported the first phantom MPI images and demonstrated the ingenuity of the method: MPI generates tomographic images by taking advantage of the nonlinear response of magnetic nanoparticles to an oscillating magnetic field to determine their spatial location and local concentration.[16] From that moment, several research groups have pursued a variety of interests in MPI, including developing tracers, improving hardware instrumentation, and enhancing image reconstruction methods. A timeline showcasing the progression of MPI as a state-of-the-art imaging method is shown in Fig. 1.

Efforts to propel MPI forward as an imaging method by improving its spatial resolution, imaging speed, and sensitivity have expanded. Although the initial MPI scanner produced high resolution images, only static images could be acquired at what was a relatively slow scanning speed.[16] In 2008, the team of Gleich and Weizenecker, together with Borgert, detailed the first experimental results for a two-dimensional fast encoding method.[54] By adding an orthogonal drive field to an MPI scanner, similar to what they used in 2005, they were able to acquire a full image in as few as 4 ms, with good quality image rendering achieved within 40 ms.[54] A year later, the first 3D real-time *in vivo* MPI scan was produced, in which details of a beating mouse heart were imaged using Resovist, a commercially available MRI contrast agent, as the magnetic tracer.[27] This was a considerable breakthrough because the spatial resolution obtained was sufficient to image heart chambers.[27] Subsequently, in 2010 an MPI scanner with an enlarged field-of-view (FOV) was constructed, providing proof that this technology can be scaled up for human use.[55]

Other MPI scanner improvements have been reported. In 2009, Goodwill *et al.*[23] introduced narrowband MPI, in which they significantly decreased the bandwidth needed for the receiver coil, giving rise to a higher signal-to-noise ratio, and established that this new MPI scanner is capable of full 3D tomographic imaging.[23] Goodwill and Conolly *et al.*[18,21] also introduced x-space MPI; its improved robustness and faster image acquisition, is ideal for real-time imaging applications. Another approach was reported by Sattel *et al.*; they fabricated a single-sided MPI device in which the object of interest is scanned from only one side, solving the problems of size limitations associated with the traditional MPI scanner.[56] Some theoretical simulations have been presented that offer improved MPI methodology. For instance, Knopp *et al.*[57] introduced field-free line formation, which helps reduce the power consumption and increase the sensitivity of MPI.

Apart from hardware improvement, the development of SPION tracers that respond strongly to an oscillating magnetic field and generate harmonics leading to an MPI signal has been essential in thrusting MPI forward as a compelling imaging modality.[26,58] Weaver *et al.*[59] obtained harmonics using magnetic particle spectroscopy (MPS) to initially study signal properties of magnetic nanoparticles. Using this analytical method, both the magnetization dynamics and the size distribution of the nanoparticles can be assessed. More recently, Weaver and his colleague Kuehlert, applied ratios of harmonic signals and a scaling law to measure the Brownian relaxation times of a ferrofluid using magnetic spectroscopy of nanoparticle Brownian motion (MSB).[60] Shortly after, Martens *et al.*[61] successfully modelled their experimental results using the Fokker–Planck formalism. Additionally, Ferguson and Krishnan *et al.* investigated the effect of SPION core size on MPI sensitivity and spatial resolution *via* a mathematical modelling approach.[22] Experimentally, they correlated the MPI signal intensity with the SPION diameter, and determined an optimal size for a particular excitation frequency.[26] In addition, Khandhar *et al.* have recently published the first paper on MPI tracers that addresses biodistribution and particokinetics in animal models.[62]

Intense interest about the research and clinical possibilities opened by MPI prompted scientists in 2010 to convene the first International Workshop on Magnetic Particle Imaging (IWMPI) to discuss progress on instrumentation and

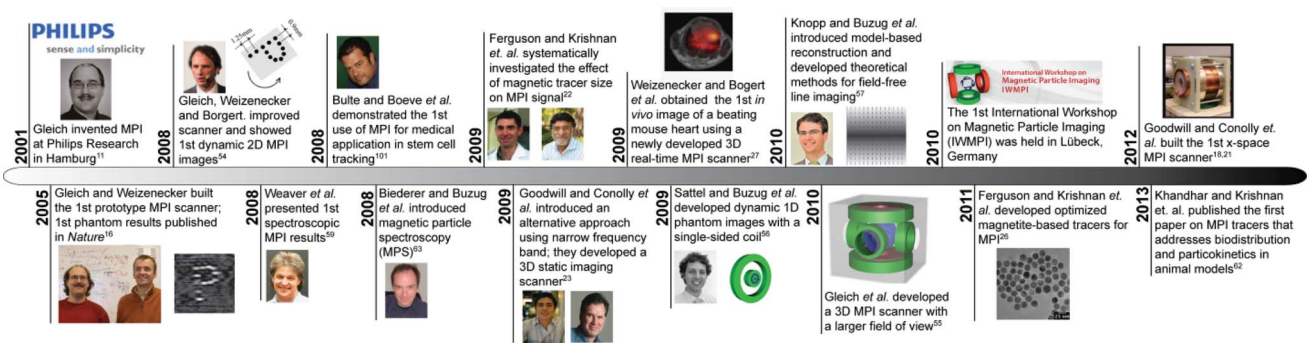

Fig. 1 Development of MPI as an imaging modality over the past decade.

tracer developments in the five years after the first published paper. All these studies and results clearly highlighted the important role that simulated analyses, instrumentation improvement, and tracer development play in designing an MPI system suitable for clinical use. In the succeeding sections of this account, we will discuss the fundamentals of MPI, cover basic principles of signal generation and acquisition, and provide an overview on image reconstruction techniques.

Signal generation and acquisition in MPI

The magnetic behavior of SPIONs is best explained by the Langevin theory, which assumes that the particles are constantly in a state of thermal equilibrium.[11] In this model, the particles are considered to be continuously moving with randomly aligned magnetic moments leading to a net zero magnetization. When an external magnetic field ($\boldsymbol{H}$) is applied, the magnetic moments of the particles align with the applied field, resulting in a net magnetization vector ($\boldsymbol{M}$). The relationship between the applied magnetic field and the resulting magnetization is nonlinear; the magnetization exhibits a steep rise in the beginning but then saturates at a particular field strength. When this point is reached, a majority of the particles are aligned with the field and further increase of the field strength will no longer alter the magnetization response of the nanoparticles. This fixed magnetization response is crucial for the spatial encoding necessary for the generation of an MPI image.[11,16,26]

On the other hand, if a time-varying magnetic field is applied, the magnetization response of the nanoparticle is delayed for a known period described by a relaxation time, τ.[11,63] At this stage, the magnetic nanoparticle can either undergo a physical particle rotation, known as Brownian rotation, or an internal magnetic moment rotation through a Néel rotation process (Fig. 2a).[64] In a fluid environment, a combination of both rotations can occur depending on the applied frequency. The relaxation time of the Néel rotation (τ_N) is described in eqn (1):[11]

$$\tau_N = \tau_0 \exp\left(\frac{K_A V}{k_B T}\right) \quad (1)$$

where K_A is the anisotropy constant, V is the nanoparticle volume, k_B is the Boltzmann constant, and T is the temperature. On the other hand, the Brownian rotation relaxation time (τ_B) is expressed in eqn (2):[11]

$$\tau_B = \frac{3\eta V_H}{k_B T} \quad (2)$$

where η is the fluid viscosity and V_H is the hydrodynamic volume. The total relaxation time is an approximated combination of both the Néel and Brownian relaxation times as described below:[22]

$$\tau = \frac{\tau_B \tau_N}{\tau_B + \tau_N} \quad (3)$$

Here, the shorter or faster relaxation process dictates the magnitude of the overall particle relaxation time, and the transition between the Néel and Brownian relaxation mechanisms depends on the nanoparticle size, the anisotropy, and on the fluidity of the particle medium.[11,22]

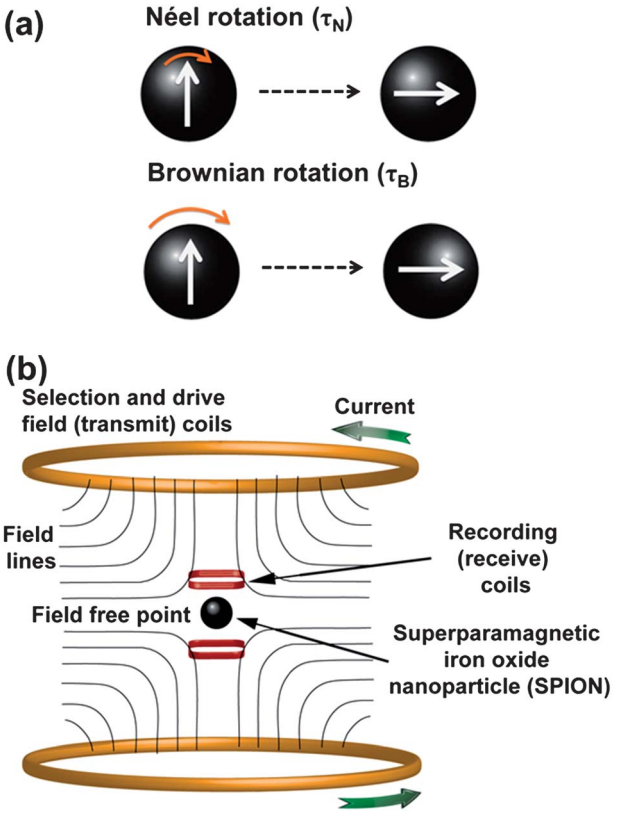

Fig. 2 Schematic representation of the magnetic relaxation mechanisms (a) and the basic components of an MPI system (b).

These relaxation properties of SPIONs in the presence of an external magnetic field provide the foundation for signal generation and acquisition in MPI. Moreover, since the particles can be stimulated to respond with a characteristic signal, this information can then be used for spatial encoding methods and image generation.

Shown in Fig. 2b are the basic components of an MPI scanner. As previously discussed, MPI applies an oscillating magnetic field (drive field) to alter the magnetization of the SPIONs using *transmit coils*.[11,16] The applied oscillating magnetic fields typically have amplitudes ranging from 0.1–20 mT.[23] To gauge the change in magnetization of the nanoparticles, the magnetic flux density is evaluated by measuring the voltage induced using appropriate *receive coils*.[11]

To determine the exact location of a magnetic nanoparticle for spatial encoding, an additional static magnetic field gradient, typically with strengths of about 4000 mT m^{-1}, is superimposed onto the drive field so that a field-free point (FFP) is established within the volume of interest.[11,17,23,27,56,65] Here, only particles located within the FFP are free to follow the excitation field and contribute to the desired signal in the *receive coils*.[11]

Since the relationship between the external applied magnetic field and the resulting SPION magnetization is

nonlinear, this leads to harmonics in the detected signal.[17] By using an appropriate signal filtering scheme, the higher order frequencies can be easily isolated from the received signal.[16] These harmonics can then be used to quantify the local concentration of the SPIONs by a simple Fourier transform as illustrated in the equation below:

$$S_n = \text{Fourier}\ \{u(t)\};\ u(t) \propto -c\mathrm{d}\boldsymbol{M}(t)/\mathrm{d}t \quad (4)$$

where S_n is the SPION harmonics, u is the voltage signal measured in the *receive coils*, c is the concentration of the SPIONs, and $\boldsymbol{M}$ is the magnetization of the nanoparticles. The generation of higher order harmonics for a nonlinear magnetization curve can be mathematically expressed by expanding the Langevin function into a Taylor series. Since all even derivatives of the Langevin function have a zero crossing point at which the Taylor series is expanded, the even harmonics are absent, and only odd harmonics are seen in the signal spectrum.[11]

At the fundamental frequency, the MPI signal is masked as a result of the excitation field and is thus undetectable.[17] The third harmonic must then be used for signal detection since it exhibits high intensity, which is characteristic of the magnetic nanoparticle particle response.[4]

Image generation in MPI

After the raw MPI signal is captured, reconstruction algorithms facilitate the conversion of the signals into images. Two principal methods of image reconstruction techniques have been reported to date: harmonic-space MPI, and x-space MPI, which are both described in the succeeding section.

Harmonic (frequency)-space MPI. The first MPI scans were obtained using an MPI imager operating in frequency space.[16,56] This mode of image reconstruction, also called harmonic-space MPI, uses a system matrix approach composed of the Fourier transform of the signal response of the SPIONs.[16,19,20]

Fig. 3 shows a schematic illustration of how signals are generated in MPI. In Fig. 3a, two magnets that are set up in a Maxwell configuration induces the FFP.[17] When the SPION tracers are situated within the FFP, a strong MPI signal is detected in the receive coil (Fig. 3b). On the other hand, the nanoparticles distant from or outside the FFP become magnetically saturated and therefore do not contribute to the MPI signal (Fig. 3c).[4] To create the tomographic image, the FFP is scanned across the sample, or the sample is moved within the selection field gradient. The harmonic response is then recorded for each FFP and a quantitative 3D scan of the magnetic tracer distribution is obtained.[23] The final image is reconstructed using matrix inversion methods.[18]

Gleich and Weizenecker[16] first applied the harmonic-space MPI method to reconstruct an image of the letter P. For their initial phantom experiment, they used undiluted Resovist and a robot to move the sample during imaging. The resulting static image obtained using this method exhibited good resolution.[16] A similar approach was later adapted to obtain the MPI scan of a mouse heart.[27]

In a harmonic-space MPI scanner, the measured signal depends on the particle concentration and the system function.[66] The system function (SF) describes the relation between the acquired MPI signal and its spatial origin.[67] The SF itself depends on the transfer function, the particle magnetization, and coil sensitivity.[66]

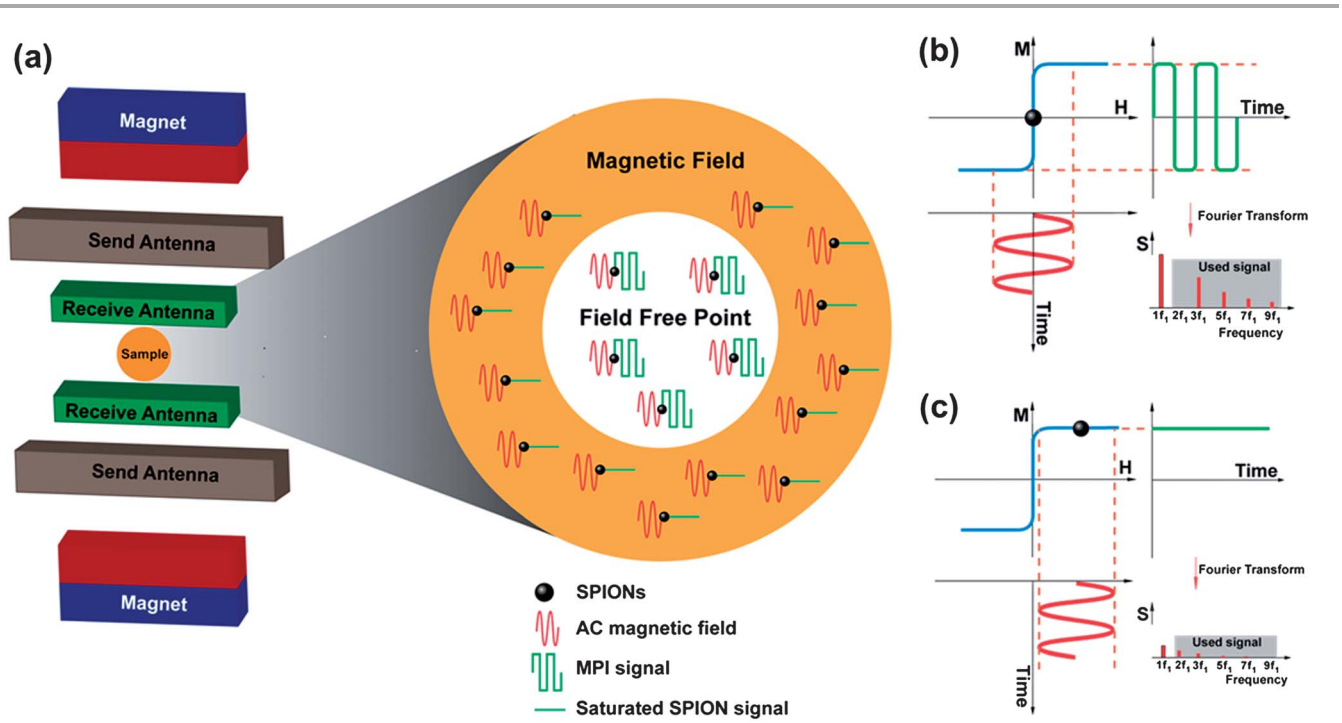

Fig. 3 Schematic illustration of signal generation in MPI (adapted from ref. 16).

To date, two different techniques have been used to acquire these parameters, namely the measurement-based and the model-based strategies.[66] In the measurement-based system function, the nanoparticle positions need to be measured several times in order to obtain high spatial resolution, a process which results in long measurement times and large data sets. Combined with high system noise, these requirements place huge demands on the hardware.[66] Conversely, the model-based system function employs mathematical calculations to simulate various parameters such as the magnetic field, particle magnetization, and the voltage induced in the receive coil.[20,68] The transfer function is estimated, by comparing the calculated data to the acquired signal at specific points, limiting the amount of data and speeding up the image acquisition process. Because the system function can be calculated within the reconstruction process, less data storage capacity is needed. However, the model-based system function results in poorer resolution compared to the measurement-based approach. Current efforts are being devoted to overcome the respective shortcomings of these two approaches. Improvements in the instrumentation as well as in the quality of the SPION tracers will further enhance the spatial and temporal resolution of the harmonic-space MPI approach.

X-space MPI. Another important imaging processing technique based on an x-space reconstruction approach was developed by the Conolly group at UC Berkeley.[18,21,23,65] In x-space MPI, three assumptions are made: (1) a strong magnetic field gradient and a uniform magnetic field form a defined FFP; (2) SPIONs can be instantaneously aligned and saturated with the applied magnetic field (>5 mT); and (3) low frequency MPI signals lost during signal detection are recovered using dynamic signal processing methods.[18,21]

In x-space MPI, the image is expressed as a convolution of the SPION spatial distribution with the point spread function (PSF) of the system. As previously described, when the FFP passes over the SPION in the sample the magnetization changes in a nonlinear fashion. Since the receive coil only detects the change in the magnetization of the particle, the PSF is in fact a derivative of the Langevin function (Fig. 4a).[18] The resulting MPI signal corresponds to a temporal scan through x-space, rather than the spatial-frequency domain used in harmonic-space MPI. In this approach, no matrix inversion is required. Instead, the image is reconstructed *via* a two-step process, which involves velocity compensation followed by instantaneous gridding of the signal to the position of the FFP (Fig. 4b).[18] Since x-space MPI only involves this two-step process, real-time image reconstruction is possible. Moreover, since no pre-characterization step is required, x-space reconstruction is a more robust MPI approach.[18]

Because the MPI scanner technologies are still in the developmental stages, only the two groups previously mentioned – Gleich's[16,54] and Conolly's[18,21,65] – have working models, the harmonic-space MPI scanner and the x-space MPI imager, respectively. For both technologies, the magnetic properties of the tracer materials determine the quality of the image resolution and the range of potential applications. Hence, alternative tracer pre-screening methods are essential to accelerate the development of the MPI technologies.

Screening of MPI tracers by magnetic particle spectroscopy (MPS)

Concurrently, magnetic particle spectroscopy (MPS) has been developed in parallel with the reconstruction of the MPI scanners to allow researchers to evaluate, characterize, and optimize the properties of tracers at a faster pace and lower costs, independent of the confounding complexities of the hardware and software technologies of a 3D MPI scanner. Without an MPS system, tracer development and optimization would be a daunting task.[62]

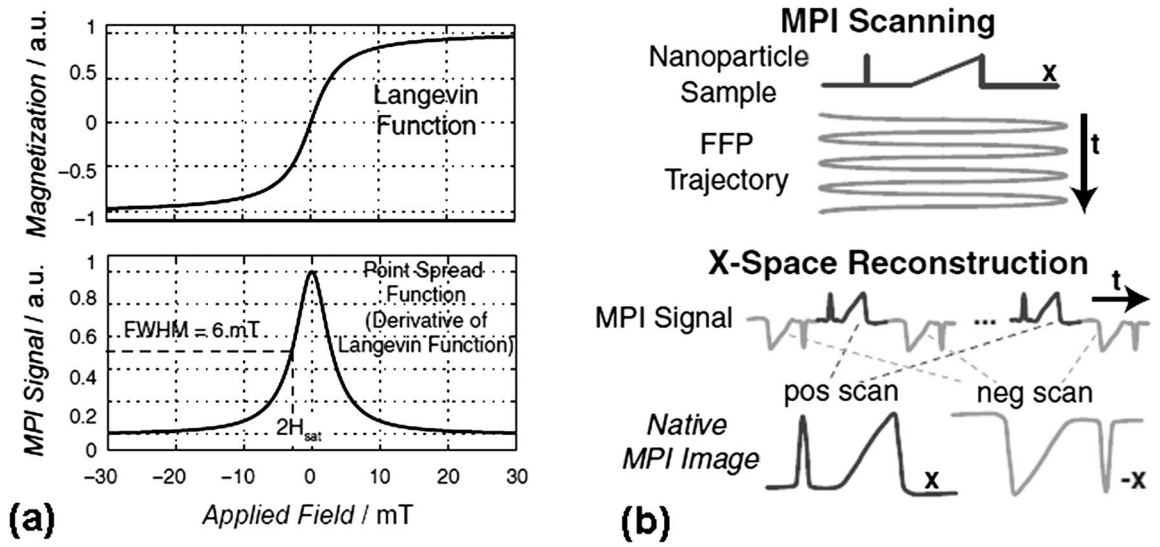

Fig. 4 Overview of the x-space image reconstruction technique. (a) Top figure shows magnetization of SPIONs modelled using a Langevin function; bottom figure shows the point spread function (PSF) as the derivative of the Langevin function; (b) x-space reconstruction involving a two-step process of velocity compensation and gridding of the instantaneous signal to the position of the FFP to form a native MPI image. (Reproduced with permission from ref. 18, Copyright 2012, John Wiley and Sons, Inc.)

An MPS system is basically a 0D analogue of an MPI scanner, which lacks the latter's spatial encoding component.[63,69] Fig. 5 is a schematic diagram of an MPS system accompanied by a flowchart of the signal detection process. The MPS is composed of concentrically arranged transmit coil and receive coil, each constructed as a solenoid, with the transmit coil serving as the outer ring. The probe chamber is located at the center of the concentric coils and is much smaller in size compared to the transmit coil's diameter, which ensures high homogeneity of magnetic field excitation within the sample.[63] To excite the magnetic nanoparticle tracer, a sine wave with frequencies typically in the 25 kHz range is generated in the transmit coil using a computer equipped with a data acquisition card. The signal from the transmit coil is further amplified and, in order to suppress background signals, a band pass filter is used.[63] To ensure that a stable and well-defined magnetic field is generated from the transmit coil for tracer excitation, the voltage produced along the transmit coil is measured and controlled by an internal feedback loop.[63] Upon excitation of the magnetic tracers, a temporal change in magnetization of the nanoparticles is detected, inducing a signal in the receive coil. Due to the coupling with the transmit coil, the fundamental frequency used to excite the nanoparticles is detected as well. Hence, a band-stop filter is employed to filter out the excitation signal.[63,70]

The data derived from MPS measurements is then used to characterize the magnetization dynamics of the SPION tracers as well as their average concentration and size distribution.[49,63] This is achieved by utilizing Langevin's theory of magnetism:

$$\boldsymbol{M}(t) = m_s c\left(\coth\left[\frac{m_s\mu_0\boldsymbol{H}(t)}{k_B T}\right] - \frac{k_B T}{m_s\mu_0\boldsymbol{H}(t)}\right) \quad (5)$$

in which μ_0 is the permeability of vacuum, k_B is the Boltzmann constant, T is the temperature in Kelvin and c is the particle concentration. The magnetic moment of saturation of the particles is given by $m_s = 1/6d\pi d_c^3\boldsymbol{M}_s$, with $\boldsymbol{M}_s$ being the saturation magnetization and d_c as the core diameter of the nanoparticle.[49]

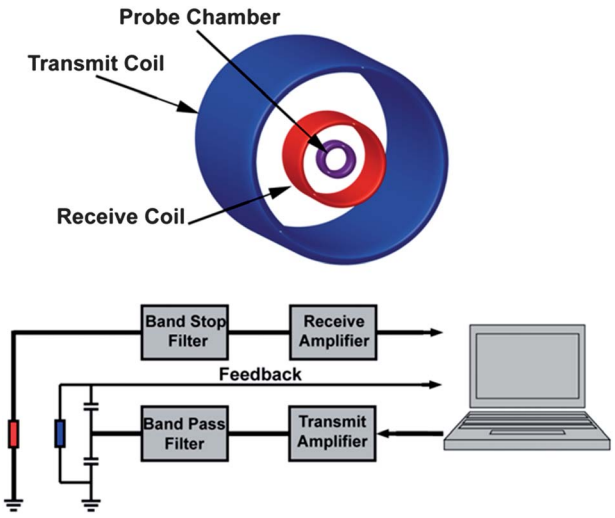

Fig. 5 Schematic diagram of a magnetic particle spectrometer (MPS) (figure adapted from ref. 63).

MPI in comparison with other imaging modalities

Various imaging platforms capture images of the structure and function of anatomical tissues in humans and other bodies. Each imaging modality differs from others in various parameters, such as spatial and temporal resolutions, sensitivity, and the mode of image rendering. Each is well-suited for some applications and poor for others. The very differentiation and abundance of imaging technologies pose conundrums for clinicians and researchers. To resolve these dilemmas, imaging systems are commonly integrated to combine strengths of the respective modalities and to reduce or eliminate weaknesses. For example, multimodal imaging platforms such as PET/CT and SPECT/CT have been widely adapted today.[71] Novel imaging techniques are continuously being developed not only to improve the visual representation of tissues and observe physiological functions but also to give us a better understanding of the mechanisms of disease and the corresponding treatment approach.[72] In most instances, contrast agents or tracers are introduced to the body to augment signal intensity and therefore provide a more detailed or enhanced image of the anatomical make-up, thus, permitting a more accurate analysis of the organ or tissue performance.

Table 1 compares key parameters of major imaging modalities with MPI, including: the type of radiation used, spatial and temporal resolution, detection sensitivity, quantitative accuracy, type of contrast agent or tracers employed, and the adapted mode of imaging – whether direct or indirect. MPI, a new and still a developing imaging technique, compares extremely well with existing imaging systems. For researchers in the biomedical community, the ideal imaging modality would have the spatial resolution of MRI, temporal resolution of ultrasound, and the sensitivity of PET.[71] The properties of MPI suggest it may approximate that ideal.

Like PET and SPECT, MPI uses tracer reagents to generate signals through which the concentration and distribution of the reagent is directly measured. But unlike in PET and SPECT the magnetic tracers used in MPI do not contain ionizing radiation. Hence, MPI is deemed to be safe for wide and frequent clinical applications; it only uses non-ionizing radiation in the form of static and oscillating magnetic fields, for which no adverse or long term effects have been reported. MRI, of course, also uses non-ionizing radiation and magnetic fields, but its measurements of magnetic nanoparticles are indirect. On the other hand, because MPI directly measures the magnetic nanoparticle concentration, it is expected to be more sensitive than MRI. Moreover, because MPI's fast imaging speed is similar to that of ultrasound, it can be used for real-time imaging.[11]

Table 1 Comparison of different imaging modalities[a]

Imaging modality	Radiation used	Spatial resolution	Temporal resolution/ acquisition time	Sensitivity	Quantifiability	Type of contrast agent/tracers	Mode of imaging
CT	X-ray	50–200 μm	Minutes	Low	Yes	Molecules with high *Z* nuclei	Indirect
PET	β/γ	1–2 mm	10 seconds to minutes	High	Yes	Radiolabeled probes	Direct
SPECT	γ	1–2 mm	Minutes	High	Yes	Radiolabeled probes	Direct
MRI	Radio waves	25–100 μm	Minutes to hours	Low	No	Paramagnetic agents	Indirect
MPI	Radio waves	200–500 μm	Seconds to minutes	High	Yes	SPIO nanoparticles	Direct

[a] Adapted from K. M. Krishnan,[4] T. F. Massoud/S. S Gambhir[72] and T. Knopp/T. M. Buzug.[11]

MPI tracer design

Since its invention, MPI has been regarded as a promising modality for theranostic research and applications. While MPI hardware design and image processing methods are essential to the features of the tomographic images generated, ultimately the quality of the images will be dictated by the characteristics of the tracers used.[51] Thus, to exploit the full potential of MPI, optimized magnetic tracers must be a focus for research and development.[26]

In previous studies, commercially available SPIONs that initially served as contrast agents for MRI, such as Resovist (Bayer Schering Pharma, Berlin) and Feridex (AMAG Pharmaceuticals, Lexington, MA), have been used in MPI scans. However, both were plagued with inhomogeneity issues, which greatly affected the quality of the harmonic spectra generated and consequently, the resulting MPI image. Additionally, Resovist and Feridex were both discontinued in the market in the late 2000s. As a result, researchers have channelled their efforts to the design of engineered magnetite-based SPIONs as promising MPI tracers.

Tracer design entails a host of vital factors, including size, surface properties, magnetic core composition, and biocompatibility – especially particle suitability for human applications.[22,50] The strength of the MPI signal and the corresponding spatial resolution are determined by the quality of the harmonic spectrum obtained, which in turn is strongly dependent on the magnetization curve of the SPION tracers. Consequently, the SPION size is a major determinant of imaging quality and performance.[4,26] As a corollary, an ideal tracer must exhibit uniform phase and size distribution of the magnetic core.[22] Uniformity in SPION ensembles is necessary to provoke simultaneous magnetization to achieve maximum signal intensity.[62] In addition, the hydrodynamic size of the SPION must also be calculated to control circulation duration in the body. Typically, particles should fall within a size range of about 15 to 100 nm to achieve optimal blood circulation.[62] Not only is particle size important, but surface coatings and attachment of target-specific moieties to the SPION must be carefully tailored. An ideal SPION tracer exhibits optimal MPI signals at low doses, circulates in the body long enough to be imaged, possesses therapeutic capabilities, and is biocompatible.

Several groups have been leading efforts to prepare optimal MPI tracers, among them Krishnan and Ferguson *et al.*,[4,22,51] Eberbeck *et al.*,[73] Markov *et al.*,[52] and Lüdtke-Buzug *et al.*[49] As previously noted, the harmonics generated are dependent on the magnetization curve of the SPIONs, which is directly related to the nanoparticle size and uniformity. Hence, it is crucial that the magnetic nanoparticles have monodisperse magnetic cores.[22] Krishnan's work demonstrated that maximum harmonic generation is achieved for monodisperse nanoparticles of a specific size at a certain excitation frequency.[22] In Krishnan's study, magnetite nanoparticles with a surfactant layer thickness of 23 nm were subjected to an applied field of 10 mT at a frequency of 50 kHz. The results revealed that both the magnetization and the third harmonic amplitude were enhanced as nanoparticle diameters increased. But at a certain point as nanoparticles continued to increase in size, magnetization and harmonic amplitude abruptly decreased as a consequence of the fast relaxation time. In addition, Krishnan's group identified an optimal particle size of about 15 nm in diameter, if K is 25 kJ m^{-3} and an RF excitation field with a 50 kHz frequency is used.[22] In another report by Ferguson and Krishnan *et al.*,[51] additional data showed that tuned magnetic nanoparticle tracers enhanced MPI performance. Fig. 6 compares MPI data obtained using the SPION tracers prepared in the Krishnan lab (UW) to commercially prepared Resovist. Transmission electron microscope (TEM) images revealed the polydispersion of the Resovist sample (Fig. 6a), in contrast to the monodisperse samples synthesized in the Krishnan lab (Fig. 6b). For both the x-space and harmonic-space measurement methodologies (Fig. 6c and d, respectively) the quality of the SPION tracer significantly influenced the measured MPI signal, with better results obtained for the monodisperse UW tracer.[74] In these figures, the particle response function (PRF) is shown, which is also regarded as a unique and fundamental property of the SPION tracers.

In addition to issues of size homogeneity, samples with strong interparticle interactions tend to agglomerate, posing serious problems for *in vivo* applications.[62] Agglomeration behavior could probably be minimized by tailoring a suitable surface coating or drug delivery vehicle. Several reports give evidence that surface functionalization of SPIONs leads to improved drug delivery and circulation by minimizing particle or tracer aggregation. Moreover, nanoparticles functionalized with fluorescent dyes, antibodies and target specific moieties have resulted in multimodal nanoplatforms that enable efficient cell uptake. For example, Lüdtke-Buzug *et al.*,[49] functionalized SPIONs with dextran and FITC and loaded them in adult stem cells for cancer therapy applications. In a similar

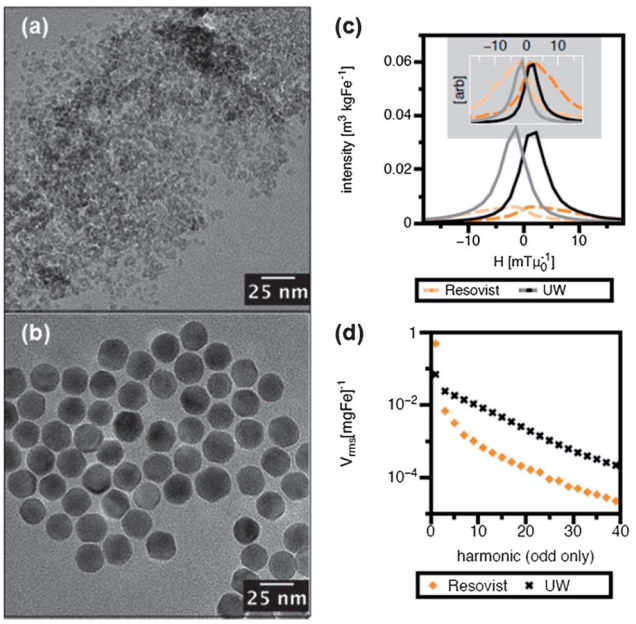

Fig. 6 TEM images of Resovist (a) and UW (b) MPI tracers (reproduced with permission from figure ref. 51, Copyright 2012, American Institute of Physics). MPS measurements taken with an excitation field of ~20 mT at 25 kHz: (c) PRF of the tracers, inset shows the normalized PRF for FWHM comparison; (d) harmonic spectra of UW tracers and Resovist, respectively. (Unpublished data reprinted with permission *via* private communication from ref. 74.)

approach, Markov *et al.*[52] loaded red blood cells with SPIONs, a technique with potential applications in cardiac disease studies. Khandhar *et al.*[62] recently reported an *in vivo* study of the biodistribution and particokinetics of SPION tracers that were optimized on rodent models. Their SPIONs exhibited lengthy blood circulation times and enhanced MPI signal generation, suggesting that the tracers can be used for angiography diagnosis and as blood-pool agents.[62]

The above studies on tracer development clearly underscore the dependence of the MPI signal strength and spatial resolution on the quality of the SPION tracers.[4] All efforts to develop ideal tracers for MPI will have to exhibit a critical understanding of the SPION core structure and composition, and carefully thought out designs for nanoparticle surfaces.

Future of MPI in diagnostics, image-guided interventions and therapy

Although MPI's translation to the clinic is still in its infancy, those working on the development of this imaging technology anticipate it will compete strongly with other imaging modalities now routinely used in disease diagnoses. In our final section, we examine potential clinical applications of MPI, including its uses in image-guided therapy and real-time *in vivo* monitoring.

Cardiovascular disease monitoring

Cardiovascular diseases (CVDs) continue to be the leading causes of deaths worldwide.[75] Despite modern progress in cardiovascular research, the timely diagnosis and treatment of atherosclerotic plaques, arterial blockages and other coronary diseases continue to be daunting challenges. The need to identify and develop new technologies that will facilitate the prevention, detection and treatment of cardiovascular ailments remains acute.[76]

Several investigators are exploring various nanoparticle carriers to treat CVD. Assessing the carrier's utility for treatment of plaque or injured blood vessels, therapeutic stent-loading, and catheter delivery remains an important task.[77–85] Engineered nanoparticles offer a plethora of opportunities for targeting the delivery of various therapeutic drugs.[78] The particle surface can host a range of functionalities through various molecular configurations and attachment of cell-specific ligands and therapeutic moieties. Magnetic nanoparticle tracers, such as Resovist, have already been used intravenously and are tailored to circulate in the bloodstream for specified lengths of time. Newly designed magnetic tracers for use with MPI make it a promising modality for monitoring blood flow and other cardiovascular structures and functions to detect CVD.[11] Because MPI generates PET-like images without tissue background and visualizes magnetic nanoparticle tracers in real-time, researchers view it as ideal for angiography and perfusion imaging in dynamic structures, vital for functional cardiac diagnostics and intervention.[86]

Traditionally, diagnostic tests for cardiovascular problems include contrast enhanced CT or CT-angiography scans, along with electrocardiography (ECG) or cardiac stress tests using SPECT or PET. In most cases, these courses of action result in lengthy diagnostic procedures that significantly delay diagnosis, and can affect the patient's chances of survival, especially in serious events such as a myocardial infarction or a heart attack. With MPI, it is possible for the coronary blood supply to be imaged while the magnetic nanoparticle tracer is flowing through the arteries, thereby simplifying the laborious and complex procedures of the standard diagnostic work-up. A proof of concept was demonstrated in a preclinical setting by Weizenecker *et al.*[27] in 2009. A mouse was injected with Resovist and inserted into the receiver coil cylinder of the MPI scanner using a cylindrical animal support to keep it supine and to ensure that the heart was within the field of view (FOV). The raw data was then obtained after bolus injection and the images reconstructed to 1800 3D volumes.[27] Since MPI does not capture the anatomical background, MR images of the mouse were also acquired to provide reference to body features. Fig. 7 shows the resulting dynamic MPI data along with the corresponding static MRI data. As shown in Fig. 7, the bolus can be seen entering the FOV *via* the *vena cava*. The resulting MPI image has very high spatial and temporal resolutions. Impressively, the image was largely obtained while the heart was actually beating, which offers evidence that MPI can be used to monitor cardiac activity in real-time.[27] These preclinical results reinforce the potential of MPI as a valuable tool in cardiac imaging and CVD diagnosis.

In addition, since MPI does not use any harmful ionizing radiation, this imaging technique would be highly beneficial to patients requiring routine examination scans. More importantly, unlike the usual coronary stress tests using SPECT or

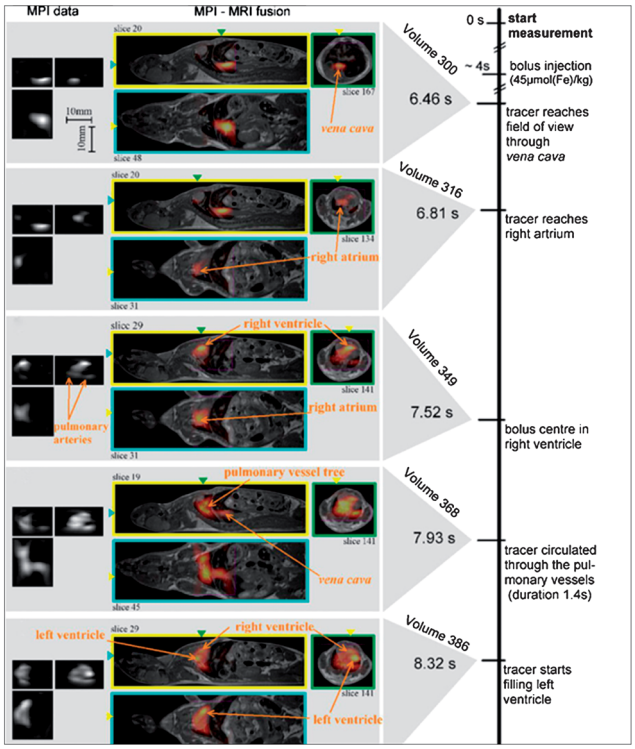

Fig. 7 Dynamic MPI images of a beating mouse heart (left) and their fusion with corresponding static MR images (right). (Reproduced with permission from ref. 27, Copyright 2009, IOP Publishing, Ltd.)

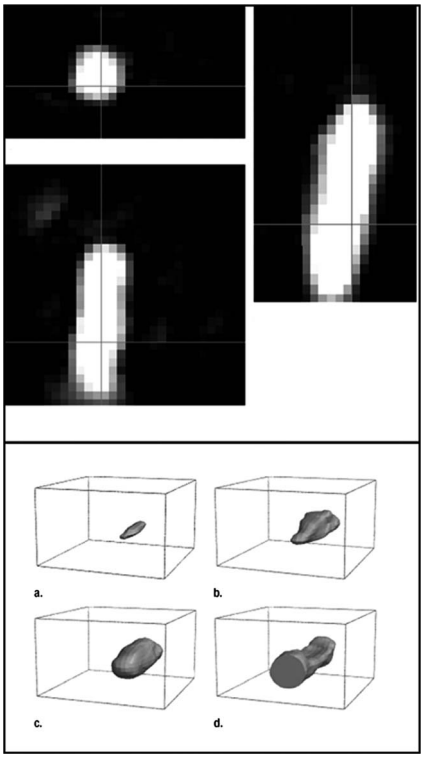

Fig. 8 MPI scans of the axial, coronal and sagittal view of Resovist-filled balloon catheter (clockwise from left, top panel). 3D rendering of the Resovist-filled balloon catheter (bottom panel): (a) deflated, (b) during inflation, (c) inflated, and (d) while being moved out of the field-of-view (FOV). (Reproduced with permission from ref. 88, Copyright 2012, Radiological Society of North America.)

PET, the heart vitality can be assessed immediately after imaging the blood supply and flow, thereby shortening the overall required time of examination. With the use of MPI in CVD detection, multiple imaging modalities and time-consuming diagnostic procedures can be decreased, resulting in reduced hospital costs, simplified diagnostic workflow, and improved overall patient comfort.[86]

In another study, Haegele *et al.* used a commercially available balloon catheter for percutaneous intraluminal angioplasty (PTA); the balloon was filled with Resovist, inserted in a vascular phantom, and imaged using an MPI scanner.[87,88] Despite the small amounts of Resovist present (Fig. 8), both the shaft and balloon were visible. The use of magnetic tracers enabled the MPI technique to monitor the insertion of the catheter, the inflation and deflation of the balloon, and the dilation of an arterial stenosis.[87] All of these capabilities are germane to balloon-expandable stent-catheters, which are routinely used for cardiovascular therapeutic interventions.

The early successes outlined above signal the probable importance of MPI in future cardiac diagnostic procedures and therapeutic interventions. For MPI to attain prime status as a major imaging modality, however, SPION tracer development will need to accelerate, and special challenges in bioengineering, such as those that would allow localized build-up or adhesion of tracers in plaques and arteries, will need to be actively explored to improve the accuracy of MPI as an imaging and monitoring tool for CVD.[52,69,87,88] Moreover, for successful implementation of MPI, human MPI scanners must become available for evaluations. Currently, MPI systems suitable for human use are actively being developed.[21,89]

Cell labelling and tracking

Magnetic iron oxide nanoparticles were first developed as contrast enhancement agents for MRI.[90–93] Over the years, these magnetic nanoparticles have since been evaluated as imaging probes to assist in targeted drug delivery and cell tracking.[49,84,94,95] Of the different types of cells currently being investigated, stem cells are regarded as among the most important, yet the most difficult to track.[11] In recent years, stem cell treatment has revolutionized regenerative medicine and cancer therapy, providing treatment for degenerative, immune and genetic diseases that were previously deemed to be incurable.[96,97]

To better understand the biodistribution dynamics and the ability of stem cells to regenerate, *in vivo* monitoring of their passage mechanisms in the blood stream is crucial. The ability to monitor stem cells as they localize to target sites is essential for the assessment of the extent of transplanted cell survival and trafficking.[94,98] In the past few years, MRI has been widely used for cell tracking and delivery,[99,100] but with the emergence of MPI, stem cell imaging and monitoring may reach a whole new level of precision.

Knopp and Buzug,[11] determined that stem cells can be loaded with up to 10 pg of iron. With MPI having a lower detection limit of 1 pg, it is conceivable that an MPI system could track a single stem cell.[11] To date, only two studies using iron oxide loaded stem cells and available experimental MPI systems have been reported. The first exploratory work was conducted by Bulte *et al.* where they detected MPI signals from neural stem cells and rat mesenchymal stem cells with clinical SPION formulations of Resovist and Feridex combined with poly-L-lysine.[101] Another study by Lüdtke-Buzug and colleagues[49] evaluated the uptake of dextran-coated SPIONs by human adult glandular stem cells and using MPS, they evaluated the SPION-loaded stem cells.

In addition to stem cells, red blood cells have also been labeled with SPIONs, with the objective to use human erythrocytes as nanoparticle carriers for MPI tracers to conduct *in vivo* monitoring of blood circulation. A study by Markov *et al.*[52] used red blood cells loaded with Resovist and Sinerem to generate the MPS signal (Fig. 9). Their results showed a weaker MPS signal for Resovist and Sinerem-loaded into red blood cells compared to the native tracers. This behavior can be attributed to the preferential encapsulation of smaller nanoparticles (with mean core diameter of 4–7 nm) inside the red blood cells.[52] The study demonstrated that SPION-loaded red blood cells generated significant MPS signals in the high frequency range while the cells without SPIONs did not show any significant signal.[52] In addition to exhibiting an MPI signal, the magnetic tracer-loaded red blood cells evidenced a long blood half-life, which makes them especially suitable for imaging of the circulatory system.[52] Thus, this preliminary study suggests that the *in vivo* real-time monitoring of the blood circulation with MPI might be used to detect blockages and other impediments in the circulatory system.

Oncology: tumor treatment and magnetic hyperthermia

Cancer diagnosis and treatment often involves surgical tumor removal followed by radiation or chemotherapy. During therapy, cancer-targeting SPIONs administered intravenously for MPI to monitor blood flow to the tumor could also assess the efficacy of the treatment.[11] Additionally, the movement of the SPION tracers to sentinel lymph nodes where metastatic cancer cells first migrate[102] could be tracked, their presence indicative of aggressive tumor progression.[103] Such tracers of cancer could reduce or obviate highly invasive and traumatic surgery to remove lymph nodes, or assure that metastases have been accurately noted and treated.[11,102,104] Currently, CT and SPECT imaging, which use dyes and radioactive tracers, are employed to locate the sentinel lymph nodes,[105] but tailored SPION tracers that preferentially target the sentinel lymph nodes can be used,[11,103,104,106] and MPI can be utilized to guide the surgery process.

In instances in which tumors or cancer cells are not accessible or amenable to surgery but can be imaged by MPI, another SPION-based therapeutic modality called magnetic hyperthermia maybe more effective or appropriate.[107,108] In magnetic hyperthermia, tumors undergo localized heating by absorbing the relaxation losses of SPION tracers in an alternating magnetic field.[4,109] SPIONs specifically tailored to target only the tumor site, coupled with MPI/hyperthermia can localize heat to the area within the FFP,[11] ensuring that tumor destruction is maximized and damage to normal tissues is prevented.

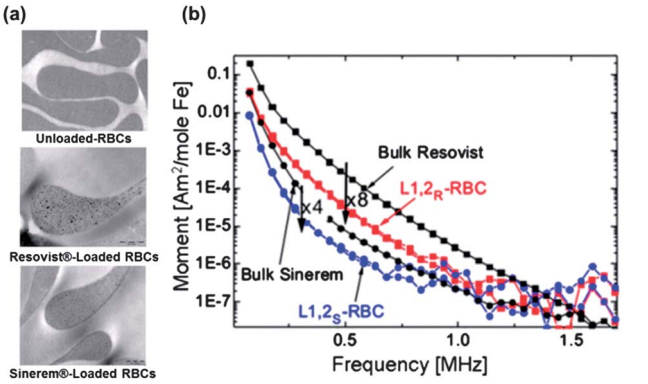

Fig. 9 (a) TEM images of unloaded and contrast-agent loaded red blood cells. (b) MPS experimental data obtained for bulk Resovist, bulk Sinerem, Resovist-loaded red blood cells ($L1,2_R$-RBC) and Sinerem-loaded red blood cells ($L1,2_S$-RBC). (Reproduced with permission from ref. 52, Copyright 2010, IOP Publishing, Ltd.)

In situ wear debris monitoring of polymer implant materials

Prosthetic implants have greatly improved the quality of life of patients, primarily because they help alleviate pain and promote mobility.[110] For high-stress applications, ultra-high molecular weight polyethylene (UHMWPE) is the polymer of choice due to its superior wear resistance and biocompatibility.[111–113] Because of the excellent physical and chemical properties of UHMWPE, it has been successfully used as bearing components in prosthetic hip and knee replacements (Fig. 10a).[114] Despite the robust features of UHMWPE, loosening and eventual failure of the implants occur. Studies have shown that polyethylene wear patterns in artificial joint replacements are not always identical and cannot be explained exclusively by mechanical factors, such as the weight and degree of physical activity of the patients.[115–117] In cases of premature and excessive wear of polyethylene bearings, chemical degradation and oxidation of the polymer can significantly lower its mechanical resistance and result in an accelerated wear-off process.[118,119] Polymer oxidation, which results in the embrittlement of the prosthetic material, can generate wear debris that eventually triggers an immune response and subsequent implant loosening (Fig. 10b).[114] This type of failure requires corrective surgery, and the added costs and risks of infection place patients in problematic situations.[110,114]

While *ex vivo* studies have been conducted on previously used polyethylene acetabular cups to understand the factors contributing to implant failure, the degradation mechanism is still not completely understood.[120,121] Under these circumstances, adaptation of MPI to provide *in situ* monitoring of wear debris from prosthetic implants will afford researchers better understanding of the process of wear and of possible avenues for mitigation. An improved assessment of the structural

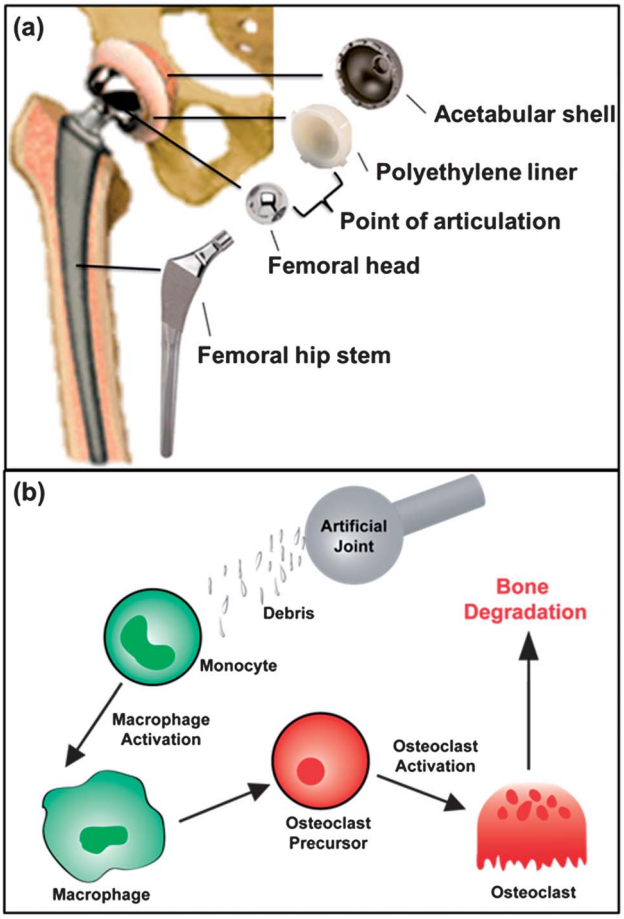

Fig. 10 (a) Basic components of a typical polyethylene knee prosthetic implant. (b) Bone degradation as a result of prosthetic implant wear debris formation.

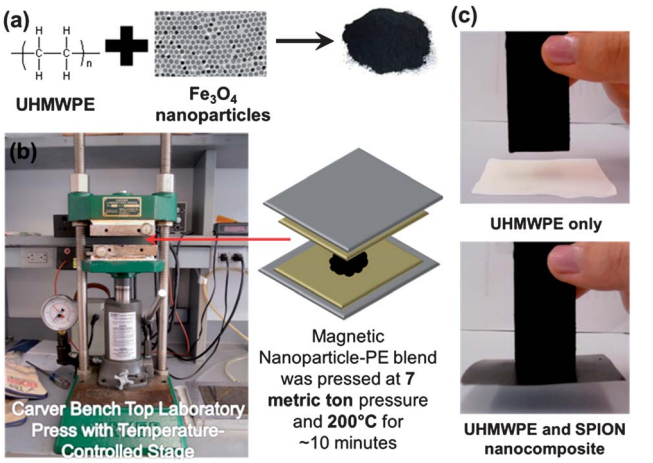

Fig. 11 (a) Components of the magnetic polymer nanocomposite used in the MPS study; (b) Carver Laboratory Press with temperature-controlled stage used in the compression molding of the nanocomposites; (c) pure UHMWPE (top) and Fe_3O_4–UHMWPE nanocomposite (bottom) films exposed to an iron–neodymium magnet.

integrity of the polyethylene subjected to mechanical and chemical stresses will provide valuable information on the material's durability, and can help predict its wear and degradation over time.

In our lab, we have begun investigating the potential application of MPI to examine composite polymer biomaterials. In particular, we are working towards the use of MPI as a unique tool to characterize the *in situ* wear debris formation of magnetic polymer nanocomposites in different chemical and biological fluid environments. To establish the feasibility of the proposed project, our research group has recently prepared a series of monodisperse Fe_3O_4 nanoparticles that could serve as magnetic components for the proposed UHMWPE nanocomposites. Using the thermal decomposition approach, we prepared high quality magnetic nanoparticles in the size range of 5–30 nm with ≤5% particle size dispersity. By mechanically mixing UHMWPE with magnetite nanoparticles (Fig. 11a), followed by compression molding at high temperature and pressure (Fig. 11b), we fabricated magnetite–UHMWPE nanocomposite films (Fig. 11c). Initial test experiments were performed to identify the composite mixing duration and compression molding conditions that resulted in visually homogeneous magnetite–UHMWPE nanocomposites. Using this approach, our group was able to fabricate a series of magnetic composite films with different loading amounts of 18 nm Fe_3O_4 nanoparticles.

Uniaxial tensile deformation studies were performed on the nanocomposites at room temperature on a Zwick-Roell Z0.5 mechanical testing machine with a 500 kN load cell and polyurethane sample grips (Fig. 12a). Dogbone films (inset, Fig. 12b) were cut from the magnetite nanocomposite films and subjected to elongation under a constant strain rate of 50% per minute. From the graph of strain *versus* standard force applied (Fig. 12b), mechanical properties such as elastic modulus and tensile strength were obtained. Previous studies have shown that the incorporation of carbon based nanomaterials such as carbon nanofibers,[122,123] graphite platelets,[124] and carbon nanotubes[125,126] within a polymeric matrix brought about enhanced elastic modulus, toughness and stiffness. These observations correlated with our experimental results in which the magnetite-loaded nanocomposites exhibited higher elastic modulus than undoped UHMWPE. In addition, magnetic hysteresis data measurements (Fig. 12c) revealed that the nanocomposites exhibited superparamagnetic behavior (zero coercivity and remanence) at room temperature. From these results we can conclude that the magnetic behavior of the nanoparticles is retained despite being subjected to high temperature and pressure.

Using a simple magnetic particle spectrometer (MPS), MPI signals were evaluated from 1 mm^2 sized magnetic nanocomposite samples with different magnetic nanoparticle loading. The MPS system used consists of a tuned, audio-frequency transmit coil and a wideband receive coil. The transmit coil consists of an amplified audio-frequency signal source and a wire-wound transmit coil tuned to the transmit frequency. The amplitude of the magnetic field generated in the transmit coil is on the order of 24 mT. On the other hand, the receive coil consists of two concentric coils with opposing windings in order to cancel the magnetic flux from the transmit

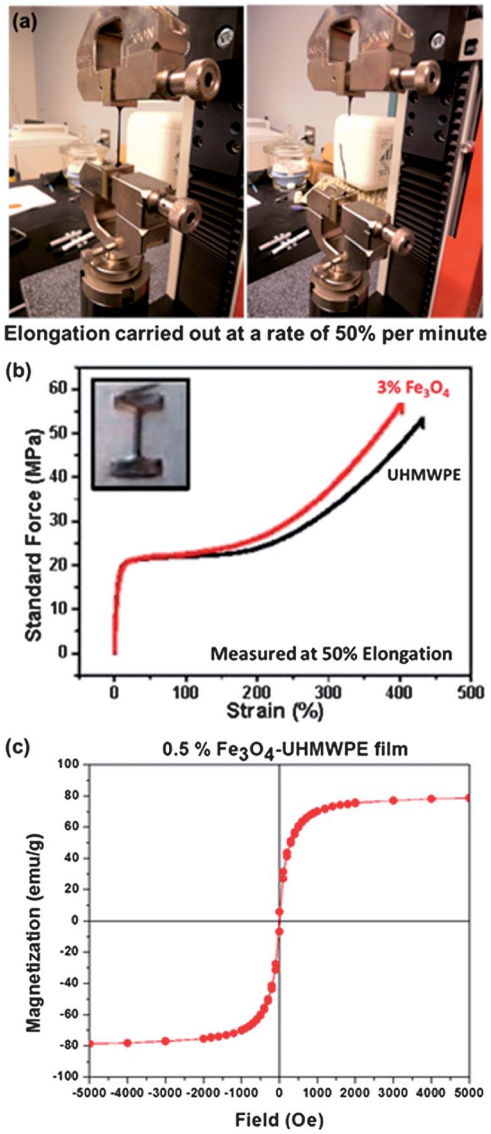

Fig. 12 (a) Mechanical testing machine showing a nanocomposite dogbone before elongation studies were carried out (left) and at the point of breakage (right); (b) plot of strain *versus* standard force obtained from elongation studies; (c) magnetic hysteresis measurement of 0.5% Fe_3O_4–UHMWPE nanocomposites obtained at 300 K showing superparamagnetic behavior.

field. During measurement, the composite sample is placed inside the receive coils. The received signal is fed through a low-pass filter to further diminish contamination from the transmit field and is finally passed to a low-noise amplifier. The harmonic spectrum is then measured by taking the fast Fourier transform (FFT) of the received signal. Using this MPS system, we were able to successfully observe signals from the fabricated nanocomposites where higher order harmonics were evident (Fig. 13).

The presence of a unique magnetic signature, as indicated by the occurrence of higher order harmonics, indicated that the magnetite–UHMWPE nanocomposites will be viable for use in prosthetic implants to facilitate *in situ* monitoring of wear debris. This approach provides a new image-guided scheme that will make real-time *in situ* monitoring of wear debris

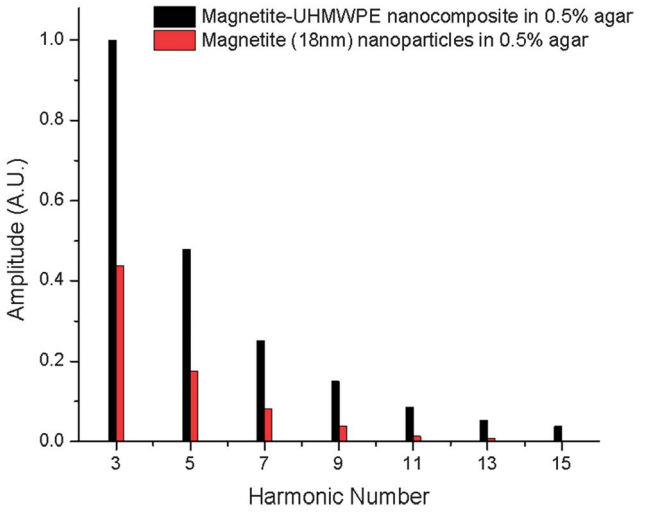

Fig. 13 Magnetic particle harmonics of magnetic polymer nanocomposites and SPIONs embedded in 0.5% agar. Measurements were obtained using a drive field of 24 mT at a frequency of 10 kHz. Amplitude was normalized with respect to 3rd harmonic of Fe_3O_4–UHMWPE nanocomposite. (Note: UHMWPE nanocomposites were loaded with 18 nm Fe_3O_4 nanoparticles; both samples contain a total of 1.5 mg Fe_3O_4 per mL agar.)

formation in different chemical and biological media a possibility. More importantly, *via* the use of the novel MPI imaging technique, this method will be able to provide helpful insights into the design and fabrication of prosthetic implants for timely monitoring and assessment, thereby preventing or limiting invasive corrective surgery.

Conclusions and future perspectives

An imaging system that has both high temporal and spatial resolution has been one of the grand aspirations in biomedicine. In this feature article, we have summarized the broad possibilities that MPI has to offer in the nascent field of theranostics. The approach of exploiting the non-linear response of superparamagnetic iron oxide nanoparticles to an oscillating magnetic field in order to generate high-resolution tomographical images is ingenious and state-of-the-art. The underlying paradigm of this concept is, without question, groundbreaking and offers extensive potential for biomedical research and development. Although it could be years before MPI is offered as a routine clinical technology, its promise as an exceptional real-time imaging modality is indisputable. The success of MPI in *in vivo* monitoring and image-guided therapy will greatly depend on the simultaneous optimization of hardware, image reconstruction algorithms, and tracers. This endeavour will involve collaborations across multiple disciplines.

Acknowledgements

The authors wish to thank L.M. Bauer and Profs M.A. Griswold, M. Martens and R. Brown of CWRU for their valuable collaboration on the MPI approach to prosthetic material study.

Moreover, we appreciatively acknowledge Prof. K.M. Krishnan and Dr R.M. Ferguson of University of Washington for sharing with us their exciting results on MPI tracer development and allowing us to include their unpublished MPS study. We also thank Prof. S. Conolly of UC Berkeley, for helpful discussions and insights on MPI. We also extend our gratitude to Prof. L. Korley, Prof. S. Rowan, Dr K. Dagnon and A. Jordan of CWRU for their assistance on mechanical testing experiments. Our study is financially supported by an IAM-IGBD Pilot Grant, an NSF-CAREER Grant (DMR-1253358) from the Solid State and Materials Chemistry Program, and a GAANN-US Fellowship for Ms. S. Situ.

Notes and references

1 D. Ho, X. Sun and S. Sun, *Acc. Chem. Res.*, 2011, **44**, 875–882.
2 R. Bardhan, S. Lal, A. Joshi and N. J. Halas, *Acc. Chem. Res.*, 2011, **44**, 936–946.
3 J. Xie, G. Liu, H. S. Eden, H. Ai and X. Chen, *Acc. Chem. Res.*, 2011, **44**, 883–892.
4 K. M. Krishnan, *IEEE Trans. Magn.*, 2010, **46**, 2523–2558.
5 R. Hao, R. Xing, Z. Xu, Y. Hou, S. Gao and S. Sun, *Adv. Mater.*, 2010, **22**, 2729–2742.
6 Y.-w. Jun, J.-H. Lee and J. Cheon, *Angew. Chem., Int. Ed.*, 2008, **47**, 5122–5135.
7 C. Rümenapp, B. Gleich and A. Haase, *Pharm. Res.*, 2012, **29**, 1165–1179.
8 D. Yoo, J.-H. Lee, T.-H. Shin and J. Cheon, *Acc. Chem. Res.*, 2011, **44**, 863–874.
9 D. Chen, X. Xia, H. Gu, Q. Xu, J. Ge, Y. Li, N. Li and J. Lu, *J. Mater. Chem.*, 2011, **21**, 12682–12690.
10 P. Howes, M. Green, A. Bowers, D. Parker, G. Varma, M. Kallumadil, M. Hughes, A. Warley, A. Brain and R. Botnar, *J. Am. Chem. Soc.*, 2010, **132**, 9833–9842.
11 T. Knopp and T. M. Buzug, in *Magnetic Particle Imaging: An Introduction to Imaging Principles and Scanner Instrumentation*, Springer, Heidelberg, New York, Dordrecht, London, 2012.
12 R. M. Botnar and M. R. Makowski, *Prog. Mol. Biol. Transl. Sci.*, 2012, **105**, 227–261.
13 J. N. Tkacz, S. A. Anderson and J. Soto, *RadioGraphics*, 2009, **29**, 1767–1780.
14 R. M. Wong, D. A. Gilbert, K. Liu and A. Y. Louie, *ACS Nano*, 2012, **6**, 3461–3467.
15 X. Chen, M.-C. Cui, W. Deuther-Conrad, Y.-F. Tu, T. Mad, Y. Xie, B. Jia, Y. Li, F. Xie, X. Wang, J. Steinbach, P. Brust, B.-L. Liu and H.-M. Jia, *Bioorg. Med. Chem. Lett.*, 2012, **22**, 6352–6357.
16 B. Gleich and J. Weizenecker, *Nature*, 2005, **435**, 1214–1217.
17 J. Borgert, J. D. Schmidt, I. Schmale, J. Rahmer, C. Bontus, B. Gleich, B. David, R. Eckart, O. Woywode, J. Weizenecker, J. Schnorr, M. Taupitz, J. Haegele, F. M. Vogt and J. Barkhausen, *Journal of Cardiovascular Computed Tomography*, 2012, **6**, 149–153.
18 P. W. Goodwill, E. U. Saritas, L. R. Croft, T. N. Kim, K. M. Krishnan, D. V. Schaffer and S. M. Conolly, *Adv. Mater.*, 2012, **24**, 3870–3877.
19 J. Weizenecker, J. Borgert and B. Gleich, *Phys. Med. Biol.*, 2007, **52**, 6363–6374.
20 T. Knopp, T. F. Sattel, S. Biederer, J. Rahmer, J. Weizenecker, B. Gleich, J. Borgert and T. M. Buzug, *IEEE Trans. Med. Imag.*, 2010, **29**, 12–18.
21 P. W. Goodwill, K. Lu, B. Zheng and S. M. Conolly, *Rev. Sci. Instrum.*, 2012, **83**, 0337081–0337088.
22 R. M. Ferguson, K. R. Minard and K. M. Krishnan, *J. Magn. Magn. Mater.*, 2009, **321**, 1548–1551.
23 P. W. Goodwill, G. C. Scott, P. P. Stang and S. M. Conolly, *IEEE Trans. Med. Imag.*, 2009, **28**, 1231–1237.
24 P. C. Lauterbur, *Nature*, 1973, **242**, 190–191.
25 G. J. Strijkers, W. J. M. Mulder, G. A. F. van Tilborg and K. Nicolay, *Anti-Cancer Agents Med. Chem.*, 2007, **7**, 291–305.
26 R. M. Ferguson, K. R. Minard, A. P. Khandhar and K. M. Krishnan, *Med. Phys.*, 2011, **38**, 1619–1626.
27 J. Weizenecker, B. Gleich, J. Rahmer, H. Dahnke and J. Borgert, *Phys. Med. Biol.*, 2009, **54**, L1–L10.
28 D. Castelli, E. Gianolio, S. G. Crich, E. Terreno and S. Aime, *Coord. Chem. Rev.*, 2008, **252**, 2424–2443.
29 K. Kim, J. H. Kim, H. Park, Y.-S. Kim, K. Park, H. Nam, S. B. Lee, J. H. Park, R.-W. Park, I.-S. Kim, K. Choi, S. Y. Kim, K. Park and I. C. Kwon, *J. Controlled Release*, 2010, **146**, 219–227.
30 K. Landfester, A. Musyanovych and V. Mailander, *J. Polym. Sci., Part A: Polym. Chem.*, 2010, **48**, 493–515.
31 S. Mornet, S. Vasseur, F. Grasset and E. Duguet, *J. Mater. Chem.*, 2004, **14**, 2161–2175.
32 C. Sun, J. S. H. Lee and M. Zhang, *Adv. Drug Delivery Rev.*, 2008, **60**, 1252–1265.
33 P. Tartaj, M. del Puerto Morales, S. Veintemillas-Verdaguer, T. Gonzalez-Carreno and C. J. Serna, *J. Phys. D: Appl. Phys.*, 2003, **36**, R182–R197.
34 B. Mehdaoui, A. Meffre, J. Carrey, S. Lachaize, L.-M. Lacroix, M. Gougeon, B. Chaudret and M. Respaud, *Adv. Funct. Mater.*, 2011, **21**, 4573–4581.
35 S. Behrens, *Nanoscale*, 2011, **3**, 877–892.
36 P. Riani, M. Napoletano and F. Canepa, *J. Nanopart. Res.*, 2011, **13**, 7013–7020.
37 A.-H. Lu, E. L. Salabas and F. Schüth, *Angew. Chem., Int. Ed.*, 2007, **46**, 1222–1244.
38 D. N. Ho, N. Kohler, A. Sigdel, R. Kalluri, J. R. Morgan, C. Xu and S. Sun, *Theranostics*, 2012, **2**, 66–75.
39 S. Sun and H. Zeng, *J. Am. Chem. Soc.*, 2002, **124**, 8204–8205.
40 J. Park, E. Lee, N.-M. Hwang, M. Kang, S. C. Kim, Y. Hwang, J.-G. Park, H.-J. Noh, J.-Y. Kim, J.-H. Park and T. Hyeon, *Angew. Chem., Int. Ed.*, 2005, **44**, 2872–2877.
41 Y. Xu, Y. Qin, S. Palchoudhury and Y. Bao, *Langmuir*, 2011, **27**, 8990–8997.
42 M. Gonzales and K. M. Krishnan, *J. Magn. Magn. Mater.*, 2005, **293**, 265–270.
43 W. W. Yu, J. C. Falkner, C. T. Yavuz and V. L. Colvin, *Chem. Commun.*, 2004, 2306–2307.
44 Q. Song, Y. Ding, Z. L. Wang and Z. J. Zhang, *J. Phys. Chem. B*, 2006, **110**, 25547–25550.

45 R. Weissleder, D. D. Stark, B. L. Engelstad, B. R. Bacon, C. C. Compton, D. L. White, P. Jacobs and J. Lewis, *Am. J. Roentgenol.*, 1989, **152**, 167–173.
46 J.-T. Jang, H. Nah, J.-H. Lee, S. H. Moon, M. G. Kim and J. Cheon, *Angew. Chem., Int. Ed.*, 2009, **48**, 1234–1238.
47 X. M. Lin and A. C. S. Samia, *J. Magn. Magn. Mater.*, 2006, **305**, 100–109.
48 Z. Feng, S. Zhu, D. R. Martins de Godoi, A. C. S. Samia and D. Scherson, *Anal. Chem.*, 2012, **84**, 3764–3770.
49 K. Lüdtke-Buzug, D. H. Rapoport and D. Schneider, Presented in Part at the 8th International Conference on the Scientific and Clinical Applications of Magnetic Carriers, Rostock, Germany, 2010.
50 N. Gehrke, A. Briel, F. Ludwig, H. Remmer, T. Wawrzik and S. Wellert, in *Magnetic Particle Imaging: A SPIO Imaging Technique*, ed. T. M. Buzug and J. Borgert, Springer Verlag, Berlin, Heidelberg, 2012, vol. 140, pp. 99–103.
51 R. M. Ferguson, A. P. Khandhar and K. M. Krishnan, *J. Appl. Phys.*, 2012, **111**, 07B3181.
52 D. E. Markov, H. Boeve, B. Gleich, J. Borgert, A. Antonelli, C. Sfara and M. Magnani, *Phys. Med. Biol.*, 2010, **55**, 6461–6473.
53 *Magnetic Particle Imaging: A Novel SPIO Imaging Technique*, ed. T. M. Buzug and J. Borgert, Springer, Heidelberg, New York, Dordrecht, London, 2012.
54 B. Gleich, J. Weizenecker and J. Borgert, *Phys. Med. Biol.*, 2008, **53**, N81–N84.
55 B. Gleich, J. Weizenecker, H. Timminger, C. Bontus, I. Schmale, J. Rahmer, J. Schmidt, J. Kanzenbach and J. Borgert, *Proc. Intl. Soc. Mag. Reson. Med.*, 2010, **18**, 218.
56 T. F. Sattel, T. Knopp, S. Biederer, B. Gleich, J. Weizenecker, J. Borgert and T. M. Buzug, *J. Phys. D: Appl. Phys.*, 2009, **42**, 022001–022005.
57 T. Knopp, T. Sattel, S. Biederer and T. M. Buzug, *J. Phys. A: Math. Theor.*, 2010, **43**, 0120021–0120029.
58 E. K. Schlachter, H. R. Widmer, A. Bregy, T. Lonnfors-Weitzel, I. Vajtai, N. Corazza, V. J. P. Bernau, T. Weitzel, P. Mordasini, J. Slotboom, G. Herrmann, S. Bogni, H. Hofmann, M. Frenz and M. Reinert, *Int. J. Nanomed.*, 2011, **6**, 1793–1800.
59 J. B. Weaver, A. M. Rauwerdink, C. R. Sullivan and I. Baker, *Med. Phys.*, 2008, **35**, 1988–1994.
60 J. B. Weaver and E. Kuehlert, *Med. Phys.*, 2012, **39**, 2765–2770.
61 M. A. Martens, R. J. Deissler, Y. Wu, L. Bauer, Z. Yao and R. Brown, *Med. Phys.*, 2013, **40**, 0223031–0223038.
62 A. P. Khandhar, R. M. Ferguson, H. Arami and K. M. Krishnan, *Biomaterials*, 2013, **34**, 3837–3845.
63 S. Biederer, T. Knopp, T. Sattel, K. Ludtke-Buzug, B. Gleich, J. Weizenecker, J. Borgert and T. M. Buzug, *J. Phys. D: Appl. Phys.*, 2009, **42**, 2050071–2050077.
64 W. T. Coffey and P. C. Fannin, *J. Phys.: Condens. Matter*, 2002, **14**, 3677–3692.
65 P. W. Goodwill and S. M. Conolly, *IEEE Trans. Med. Imag.*, 2010, **29**, 1851–1859.
66 M. Graeser, S. Biederer, M. Gruttner, H. Wojtczyk, T. Sattel, W. Tenner, G. Bringout and T. M. Buzug, in *Magnetic Particle Imaging: A Novel SPIO Imaging Technique*, ed. T. M. Buzug and J. Borgert, Springer Verlag, Berlin, Heidelberg, 2012, vol. 140, pp. 59–64.
67 J. Rahmer, J. Weizenecker, B. Gleich and J. Borgert, *IEEE Trans. Med. Imag.*, 2012, **31**, 1289–1299.
68 T. Knopp, S. Biederer, T. Sattel, J. Rahmer, J. Weizenecker, B. Gleich, J. Borgert and T. M. Buzug, *Med. Phys.*, 2010, **37**, 485–491.
69 J. Haegele, S. Biederer, H. Wojtczyk, M. Graser, T. Knopp, T. M. Buzug, J. Barkhausen and F. M. Vogt, *Magn. Reson. Med.*, 2012, 1–7.
70 F. Ludwig, T. Wawrzik and M. Schilling, in *Magnetic Particle Imaging*, ed. T. M. Buzug and J. Borgert, Springer Verlag, Berlin, Heidelberg, 2012, vol. 140, pp. 35–40.
71 S. R. Cherry, *Annu. Rev. Biomed. Eng.*, 2006, **8**, 35–62.
72 T. F. Massoud and S. S. Gambhir, *Genes Dev.*, 2003, **17**, 545–580.
73 D. Eberbeck, F. Wiekhorst, S. Wagner and L. Trahms, *Appl. Phys. Lett.*, 2011, **98**, 1825021–1825023.
74 R. M. Ferguson and K. M. Krishnan, unpublished work.
75 V. L. Roger, A. S. Go, D. M. Lloyd-Jones, R. J. Adams, J. D. Berry, T. M. Brown, M. R. Carnethon, S. Dai, G. de Simone, E. S. Ford, C. S. Fox, H. J. Fullerton, C. Gillespie, K. J. Greenlund, S. M. Hailpern, J. A. Heit, P. M. Ho, V. J. Howard, B. M. Kissela, S. J. Kittner, D. T. Lackland, J. H. Lichtman, L. D. Lisabeth, D. M. Makuc, G. M. Marcus, A. Marelli, D. B. Matchar, M. M. McDermott, J. B. Meigs, C. S. Moy, D. Mozaffarian, M. E. Mussolino, G. Nichol, N. P. Paynter, W. D. Rosamond, P. D. Sorlie, R. S. Stafford, T. N. Turan, M. B. Turner, N. D. Wong and J. Wylie-Rosett, *Circulation*, 2011, **123**, e18–e209.
76 T. Quillard and P. Libby, *Circ. Res.*, 2012, **111**, 231–244.
77 J. Meng, X.-D. Yang, L. Jia, X.-J. Liang and C. Wang, *Curr. Drug Metab.*, 2012, **13**, 1123–1129.
78 P. Galvin, D. Thompson, K. B. Ryan, A. McCarthy, A. C. Moore, C. S. Burke, M. Dyson, B. D. MacCraith, Y. K. Gun'ko, M. T. Byrne, Y. Volkov, C. Keely, E. Keehan, M. Howe, C. Duffy and R. MacLoughlin, *Cell. Mol. Life Sci.*, 2012, **69**, 389–404.
79 L. Brito and M. Amiji, *Int. J. Nanomed.*, 2007, **2**, 143–161.
80 R. Tong and J. Cheng, *Angew. Chem., Int. Ed.*, 2008, **47**, 4830–4834.
81 K. Park, H.-Y. Hong, H. J. Moon, B.-H. Lee, I.-S. Kim, I. C. Kwon and K. Rhee, *J. Controlled Release*, 2008, **128**, 217–223.
82 S. A. Wickline, A. M. Neubauer, P. M. Winter, S. D. Caruthers and G. M. Lanza, *J. Magn. Reson. Imag.*, 2007, **25**, 667–680.
83 A. Heidsieck, S. Vosen, K. Zimmermann, D. Wenzel and B. Gleich, *Mol. Pharmaceutics*, 2012, **9**, 2029–2038.
84 D. A. Kedziorek and D. L. Kraitchman, in *Stem Cells for Myocardial Regeneration: Methods and Protocols, Methods in Molecular Biology*, ed. R. J. Lee, Springer-Science Business Media, LLC, 2010, vol. 660.
85 K. S. Kim, G. Khang and D. Lee, *Curr. Pharm. Des.*, 2011, **17**, 1825–1833.

86 G. Schutz, in *Magnetic Particle Imaging: A Novel SPIO Imaging Technique*, ed. T. M. Buzug and J. Borgert, Springer Verlag, Berlin, Heidelberg, 2012, vol. 140, pp. 129–134.
87 J. Haegele, J. Rahmer, B. Gleich, C. Bontus, J. Borgert, H. Wojtczyk, T. M. Buzug, J. Barkhausen and F. M. Vogt, in *Magnetic Particle Imaging: A Novel SPIO Imaging Technique*, ed. T. M. Buzug and J. Borgert, Springer Verlag, Berlin, Heidelberg, 2012, vol. 140, pp. 211–215.
88 J. Haegele, J. Rahmer, B. Gleich, J. Borgert, H. Wojtczyk, N. Panagiotopoulos, T. M. Buzug, J. Barkhausen and F. M. Vogt, *Radiology*, 2012, **265**, 933–938.
89 P. W. Goodwill and S. M. Conolly, Medical imaging 2011: biomedical applications in molecular, structural, and functional imaging, *Proc. SPIE*, 2011, **7965**, 79650U79651–79650U79656.
90 E. Canet, D. Revel, R. Forrat, C. Baldy-Porcher, M. de Lorgeril, L. Sebbag, J. P. Vallee, D. Didier and M. Amiel, *Magn. Reson. Imaging*, 1993, **11**, 1139–1145.
91 T. Bach-Gansmo, A. K. Fahlvik, A. Ericsson and A. Hemmingsson, *Invest. Radiol.*, 1994, **29**, 339–344.
92 B. Bonnemain, *J. Drug Targeting*, 1998, **6**, 167–174.
93 H. Lee, H. Shao, Y. Huang and B. Kwak, *IEEE Trans. Magn.*, 2005, **41**, 4102–4104.
94 R. M. Guo, N. Cao, F. Zhang, Y. R. Wang, X. H. Wen, J. Shen and X. T. Shuai, *Eur. J. Radiol.*, 2012, **22**, 2328–2337.
95 A. Fernandez-Fernandez, R. Manchanda and A. J. McGoron, *Appl. Biochem. Biotechnol.*, 2011, **165**, 1628–1651.
96 M. Mimeault and S. K. Batra, *Stem Cells*, 2006, **24**, 2319–2345.
97 M. Mimeault, R. Hauke and S. K. Batra, *Clin. Pharmacol. Ther.*, 2007, **82**, 252–264.
98 J. W. Bulte, *Am. J. Roentgenol.*, 2009, **193**, 314–325.
99 M. Y. Emmert, P. Wolint, S. Winklhofer, P. Stolzmann, N. Cesarovic, T. Fleischmann, T. D. L. Nguyen, T. Frauenfelder, R. Boni, J. Scherman, D. Bettex, J. Grunenfelder, R. Schwartlander, V. Vogel, M. Gyongyosi, H. Alkadhi, V. Falk and S. P. Hoerstrup, *Biomaterials*, 2013, **34**, 2428–2441.
100 E. Amstad, M. R. Textor and E. Reimhult, *Nanoscale*, 2011, **3**, 2819–2843.
101 J. W. Bulte, B. Gleich, J. Weizenecker, S. Bernard, P. Walczak, D. E. Markov, H. C. Aerts, J. Borgert and H. Boeve, Developing Cellular MPI: Initial Experience, in *Proceedings of ISMRM*, vol. 16, p. 1675, Toronto, 2008.
102 R. L. Ferris, M. T. Lotze, S. P. L. Leong, D. S. B. Hoon and D. L. Morton, *Clin. Exp. Metastasis*, 2012, **29**, 729–736.
103 C. Niu, Z. Wang, G. Lu, T. M. Krupka, Y. Sun, Y. You, W. Song, H. Ran, P. Li and Y. Zheng, *Biomaterials*, 2013, **34**, 2307–2317.
104 D. Finas, K. Baumann, K. Heinrich, B. Ruhland, L. Sydow, K. Grafe, T. Sattel, K. Ludtke-Buzug and T. M. Buzug, in *Magnetic Particle Imaging: A Novel SPIO Imaging Technique*, ed. T. M. Buzug and J. Borgert, Springer Verlag, Berlin, Heidelberg, 2012, pp. 187–191.
105 U. Veronesi, G. Paganelli, G. Viale, V. Galimberti, A. Luini, S. Zurrida, C. Robertson, V. Sacchini, P. Veronesi, E. Orvieto, C. De Cicco, M. Intra, G. Tosi and D. Scarpa, *J. Natl. Cancer Inst.*, 1999, **91**, 368–373.
106 A. Saokar, M. Braschi and M. Harisinghani, *Abdom. Imag.*, 2006, **31**, 660–667.
107 A. S. Jordan, R. Scholz, P. Wust, H. Fähling, J. Krause, W. Wlodarczyk, B. Sander, T. Vogl and R. Felix, *Int. J. Hyperthermia*, 1997, **13**, 587–605.
108 A. P. Khandhar, R. M. Ferguson, J. A. Simon and K. M. Krishnan, *J. Appl. Phys.*, 2012, **111**, 07B3061.
109 A. P. Khandhar, R. M. Ferguson, J. A. Simon and K. M. Krishnan, *J. Biomed. Mater. Res., Part A*, 2012, **100A**, 728–737.
110 E. N. Taylor and T. J. Webster, *Int. J. Nanomed.*, 2009, **4**, 145–152.
111 S. M. Kurtz, *The UHMWPE Handbook: Ultra-High Molecular Weight Polyethylene in Total Joint Replacement*, Elsevier Academic Press, San Diego, CA, 2004.
112 E. M. Brach del Prever, A. Bistolfi, P. Bracco and L. Costa, *Journal of Orthopaedics and Traumatology*, 2009, **10**, 1–8.
113 E. Gomez-Barrena, J.-A. Puertolas, L. Munuera and Y. T. Konttinen, *Acta Orthop.*, 2008, **79**, 832–840.
114 H. Bhatt and T. Goswami, *Biomed. Mater.*, 2008, **3**, 1–9.
115 M. F. Rocha, A. A. P. Mansur and H. S. Mansur, *Macromol. Symp.*, 2010, **296**, 487–492.
116 M. F. G. Rocha, A. A. P. Mansur, C. P. S. Martins, E. F. Barbosa-Stancioli and H. S. Mansur, *Open Biomed. Eng. J.*, 2010, **4**, 107–112.
117 S. Li, J. D. Chang, E. G. Barrena, B. D. Furman, T. M. Wright and E. Salvati, *Clin. Orthop. Relat. Res.*, 1995, **319**, 54–63.
118 S. M. Kurtz, M. S. Austin, K. Azzam, P. F. Sharkey, D. W. MacDonald, F. J. Medel and W. J. Hozack, *J. Arthroplasty*, 2010, **25**, 614–623.
119 B. H. Currier, J. H. Currier, M. B. Major, K. A. Lyford, J. P. Colier and D. W. Van Citters, *J. Bone Jt. Surg., Am. Vol.*, 2007, **89**, 2023–2029.
120 J. A. Savio, L. M. Overcamp and J. Black, *Clin. Mater.*, 1994, **12**, 1–47.
121 J. Fisher, H. M. McEwen, J. L. Tipper, A. L. Galvin, J. Ingram, A. Kamali, M. J. Stone and E. Ingham, *Clin. Orthop. Relat. Res.*, 2004, **428**, 114–119.
122 W. J. Wood, R. G. Maguire and W. H. Zhong, *Composites, Part B*, 2011, **42**, 584–591.
123 M. C. Galetz, T. Blab, H. Ruckdaschel, J. K. W. Sandler, V. Altstadt and U. Glatzel, *J. Appl. Polym. Sci.*, 2007, **104**, 4173.
124 A. Delgado, F. Addiego, S. Ahzi, S. Patlazhan, V. Toniazzo and D. Ruch, *IOP Conf. Ser.: Mater. Sci. Eng.*, 2012, **31**, 1–6.
125 J.-H. Lee, J. Kathi, K. Y. Rhee and J. H. Lee, *Polym. Eng. Sci.*, 2010, 1433–1439.
126 J. F. Vega, J. Martinez-Salazar, M. Trujillo, M. L. Arnal, A. J. Muller, S. Bredeau and P. Dubois, *Macromolecules*, 2009, **42**, 4719–4727.